ACS APPLIED MATERIALS & INTERFACES
Research Article
www. acsami. org

Effect of Graphene Layer Thickness and Mechanical Compliance on Interfacial Heat Flow and Thermal Conduction in Solid–Liquid Phase Change Materials

Ronald J. Warzoha[†] and Amy S. Fleischer*

Department of Mechanical Engineering, Villanova University, 830 Lancaster Avenue, Villanova, Pennsylvania 19010, United States

Supporting Information

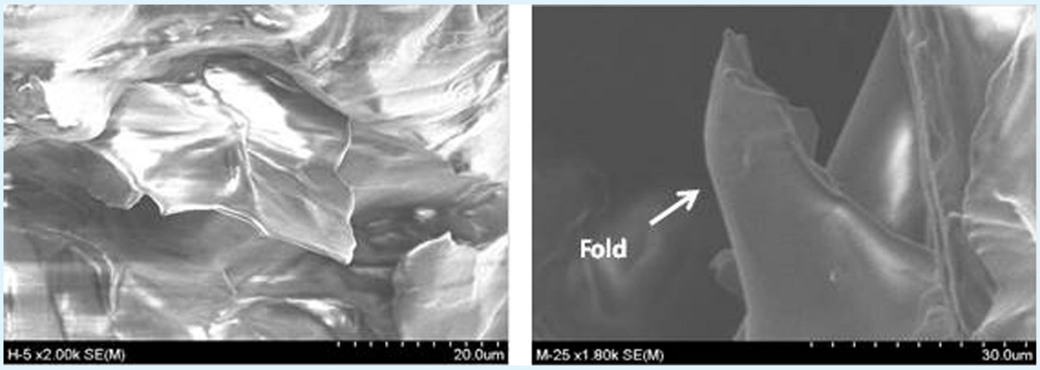

ABSTRACT: Solid–liquid phase change materials (PCMs) are attractive candidates for thermal energy storage and electronics cooling applications but have limited applicability in state-of-the-art technologies due to their low intrinsic thermal conductivities. Recent efforts to incorporate graphene and multilayer graphene into PCMs have led to the development of thermal energy storage materials with remarkable values of bulk thermal conductivity. However, the full potential of graphene as a filler material for the thermal enhancement of PCMs remains unrealized, largely due to an incomplete understanding of the physical mechanisms that govern thermal transport within graphene-based nanocomposites. In this work, we show that the number of graphene layers (n) within an individual graphene nanoparticle has a significant effect on the bulk thermal conductivity of an organic PCM. Results indicate that the bulk thermal conductivity of PCMs can be tuned by over an order of magnitude simply by adjusting the number of graphene layers (n) from $n = 3$ to 44. Using scanning electron microscopy in tandem with nanoscale analytical techniques, the physical mechanisms that govern heat flow within a graphene nanocomposite PCM are found to be nearly independent of the intrinsic thermal conductivity of the graphene nanoparticle itself and are instead found to be dependent on the mechanical compliance of the graphene nanoparticles. These findings are critical for the design and development of PCMs that are capable of cooling next-generation electronics and storing heat effectively in medium-to-large-scale energy systems, including solar–thermal power plants and building heating and cooling systems.

KEYWORDS: *graphene, layer number, compliance, nanocomposite, thermal conduction, thermal conductivity, interfacial thermal resistance*

INTRODUCTION

The efficient removal and recovery of heat is critical for the development of next-generation integrated circuitry and waste heat recovery systems. Accordingly, an increased emphasis has been placed on the development of novel materials that can store and transmit energy passively (i. e., without the need for external power consumption). Solid–liquid phase change materials (PCMs) can absorb and shed large amounts of heat during a constant-temperature phase transition, making them excellent candidates for passive thermal abatement and energy harvesting in electronics cooling and waste heat recovery systems, respectively.[1−5] Unfortunately, PCMs have limited applicability in state-of-the-art energy and electronics systems due to their inherently low thermal conductivities (on the order of 0.1 W/mK). This issue can result in a rapid temperature overshoot within the PCM (and, consequently, electronic device failure)[6,7] or low power capacities for thermal energy storage applications.[8] Fittingly, many works have therefore focused on the development of novel filler materials in order to enhance the PCM's thermal conductivity.

Traditional filler materials, such as copper fins[9] and carbon foams,[5,10] offer increased PCM thermal conductivity but are limited by manufacturing constraints and ligament thermal conductivity. Foam ligaments have also been shown to suppress

Received: May 8, 2014
Accepted: July 1, 2014
Published: July 1, 2014

Table 1. Thermal Conductivity Enhancements of Bulk Materials Due to the Presence of Graphene Nanofillers

graphene filler type[a]	thickness (nm)	matrix material	concentration (max reported)[b]	enhancement[c] (%)	ref
GN	2	epoxy	25 vol %	3000	19
MLG	4−20	paraffin	10 wt %	400	20
MLG	420	paraffin	5 wt %	164	21
SLG	0.4	epoxy	5 vol %	500	22
SLG	0.4	silver epoxy	5 vol %	1000	22
SLG/MLG	0.4−2.5	epoxy	10 vol %	2300	23

[a] GN = graphite nanoplatelet, SLG = single layer graphene, MLG = multilayer graphene. [b] vol % = volume percent, wt % = weight percent. [c] $(((k_e - k_m)k_e - k_m/k_m)) \times 100\%)$, where k_m is the bulk material thermal conductivity

natural convection (i. e., buoyant fluid movement) within the PCM during the melt phase and therefore reduce the rate of melt front propagation. Consequently, researchers have turned their attention to high thermal conductivity, carbon-based nanoparticles (such as CNTs and graphene) as filler materials. This is primarily due to recent work that reports record-high intrinsic thermal conductivities for carbon-based nanoparticles (up to 6000 W/mK).[11,12] Using a standard mixing approximation for materials having continuous, percolating fillers (eq 1),[13] one can calculate an expected thermal conductivity of a PCM embedded with carbon nanoparticles.

$$k_e = \phi_{PCM} k_{PCM} + \phi_{np} k_{np} \quad (1)$$

In eq 1, k_e represents the effective thermal conductivity of the composite, k_{PCM} and k_{np} are the intrinsic thermal conductivities of the PCM and nanoparticle, respectively, and ϕ_{PCM} and ϕ_{np} are the volume concentrations of both the PCM and nanoparticle. This equation is often used to exemplify the potential of carbon-based nanoparticles as constituents for the thermal enhancement of bulk materials. For example, if we assume that a bulk paraffin PCM (where $k_{paraffin}$ = 0.25 W/mK[14]) contains a volume concentration of 10%, atomically thick graphene nanoparticles [in general, we define a graphene nanoparticle as a two-dimensional sheet of carbon having a thickness less than 100 nm] (where $k_{graphene}$ = 5300 W/mK[15]), an effective thermal conductivity of ∼530 W/mK is expected for the paraffin nanocomposite based on eq 1 (or over an order of magnitude greater than what can be achieved with graphite foams[16]). To date, no single study has been able to achieve such an enhancement for any type of bulk material when using graphene as a filler particle. However, recent molecular dynamics simulations suggest that the formation of an atomic level ordering of alkane molecules across a graphene nanoparticle's primary face(s)[17,18] results in better thermal coupling at graphene−paraffin interfaces and therefore greater enhancements in bulk PCM thermal conductivity. For reference, a cursory survey of the magnitude enhancement that has been achieved in the bulk thermal conductivity of different materials through the incorporation of graphene constituents is given in Table 1.

Although the data in Table 1 suggest that the thermal conductivity of a bulk material is significantly increased with the inclusion of graphene nanoparticles, the mixing approximation provided in eq 1 can be used to show that the expected thermal conductivity enhancement should be between 1 and 2 orders of magnitude higher than it is. This is true even when the intrinsic, in-plane thermal conductivity of the graphene nanoparticles is reduced due to ZA phonon damping when embedded within a bulk material (or attached to a substrate).[15,24] The damping of ZA phonons, which is due primarily to differences in the phonon density of states between the graphene nanoparticle and the surrounding material, was theoretically predicted to result in an ∼20−50% decrease in the intrinsic thermal conductivity of thin films (like atomically thick graphene) over a decade ago.[25] Recently, Seol et al.[26] experimentally confirmed these theoretical predictions. The authors found that the thermal conductivity of atomically thick graphene on SiO_2 is ∼600 W/mK at room temperature (300 K). Although this value is significantly less than what is observed for suspended graphene (∼3000−5300 W/mK[12]), it still exceeds the thermal conductivities of most common heat transfer metals, including copper (oxygen-free, high conductivity copper, for instance, has a thermal conductivity on the order of ∼400 W/mK[27]). Additionally, the intrinsic thermal conductivity of supported graphene is expected to scale as $k_{graphene} \sim \ln(n)$, where k increases as the number of graphene layers, n, increases. Eventually, the intrinsic thermal conductivity of graphene approaches the bulk thermal conductivity of graphite.[15] Conversely, the thermal conductivity of suspended graphene is shown to increase with decreasing layer number. Given the unique nature with which the alkane molecules in paraffin-type PCMs are expected to behave at graphene interfaces,[17] it is unclear whether the bulk thermal conductivity of a paraffin PCM embedded with graphene nanoparticles will increase or decrease upon increasing or decreasing graphene layer number. Nevertheless, paraffin's high affinity for graphene is not expected to result in a thermal conductivity lower than that of graphene on SiO_2. Thus, the enhancement factors provided in Table 1 are still at least an order of magnitude lower than what is predicted for composites with embedded graphene nanoparticles.

The physical mechanisms responsible for these underwhelming results are still not fully understood. However, several experimental and computational efforts generally point to the existence of an interfacial thermal resistance between the nanoparticles and the matrix and/or between contacting nanoparticles,[24,28−30] which results in less net heat flow across the nanocomposite. More recent efforts in this area have identified some of the physical and chemical mechanisms responsible for the existence of this interfacial thermal resistance, including: the contacting geometry, the strength of chemical bonds at nanoparticle interfaces, and the mismatch in the phonon density of states at nanoparticle interfaces.[31] However, it is unclear whether: (1) this interfacial thermal resistance has a larger effect than any reduction in the thermal conductivity of graphene due to flexural ZA phonon suppression and (2) what physical mechanisms are most responsible for the interfacial thermal resistance in graphene−PCM composites. To successfully utilize nanoparticles to enhance bulk material thermal conductivity, it will be critical to identify the physical mechanisms that are most responsible for these limitations. Consequently, it is imperative to determine the effects of intrinsic nanoparticle thermal conductivity and nanoparticle geometry (effective diameter(s) and thickness) on a PCM's bulk and nano scale thermal behavior.

In this work, we examine the influence of graphene layer number (n = 3−44) on the thermal conductivity of a bulk, amorphous PCM (paraffin, IGI 1230A) and on the interfacial thermal resistance at graphene−graphene junctions when graphene percolates throughout the paraffin matrix. The geometric and mechanical properties for each type of commercial graphene nanoparticles that are used in this study are given in Table 2. In total, nine different variations of few-layer graphene nanoparticles (FLG, XG Sciences) are used in this work to produce nanocomposites with volume concentrations ranging from 0.01 to 20 vol % (details of sample preparation can be found in the Experimental Section). Of note is the relationship between the calculated layer number for each type of graphene nanoparticle and its corresponding bending stiffness, C (Table 2). As shown in Table 2, as the number of graphene layers decreases, so too does the nanoparticle's bending stiffness. For monatomic graphene, it has been reported that the bending stiffness reaches 1.44 eV, which leads to a high degree of folding under mechanical and/or thermal loading.[32]

Table 2. Geometrical Properties of Nine Different Few-Layer Graphene Types

graphene type	diameter(s) (μm)	thickness (nm)	calculated layer number (n)[a]	bending stiffness,[33] C[b] (eV)
c-750, c-500, c-300	1.5	1|2|3	3|6|9	1400|4200|14000
m-5, m-15, m-25	5, 15, 25	7	20	74000
h-5, h-15, h-25	5, 15, 25	15	44	380000

[a] Layer number is calculated as $n = t/h$, where t is thickness and h = 0.34 nm.[34] The calculated layer number is rounded to the nearest whole number. [b] The isotropic bending stiffness, C, is determined according to the details provided in ref 29. This value is meant to indicate the magnitude difference in bending stiffness between the different graphene nanoparticles with different thicknesses and should not be taken as an exact value.

■ RESULTS AND DISCUSSION

Parts a and b of Figure 1 show the influence of graphene nanoparticle loading level and geometry on the thermal conductivity of a commercial paraffin PCM (IGI 1230A), which is measured via the Transient Plane Source technique. In contrast to other work[23] (which does not definitively distinguish between the dilute and percolating regime due to the small range of nanoparticle concentrations used), it is apparent that a "kink" in the thermal conductivity distribution exists for the m-type graphene−paraffin nanocomposites (Figure 1a,b), revealing a shift from the dilute regime to the percolating regime at ~0.9 vol %. The percolation threshold is also determined for each of the other nanocomposite PCMs by examining this type of departure (see Figure S1 in Supporting Information). The percolation threshold for the h-type and c-type nanoparticles is found to exist at ~2.5 vol %. Therefore, the thermal conductivity data in Figure 1a (i. e., from 0 to 0.9 vol %) are used to evaluate the interfacial thermal resistance between each type of graphene nanoparticle and paraffin, while the thermal conductivity data at concentrations ranging from 2.5 to 20 vol % are used to calculate the interfacial thermal resistance between contacting graphene nanoparticles. Digital optical microscopy is used to validate these ranges by ensuring that a dilute regime exists (i. e., all graphene nanoparticles are separated from one another) prior to 1 vol % (see Figure S2 in Supporting Information). It should be noted that the standard deviation in the reported thermal conductivity in Figure 1 is less than 6.4% for all composite types.

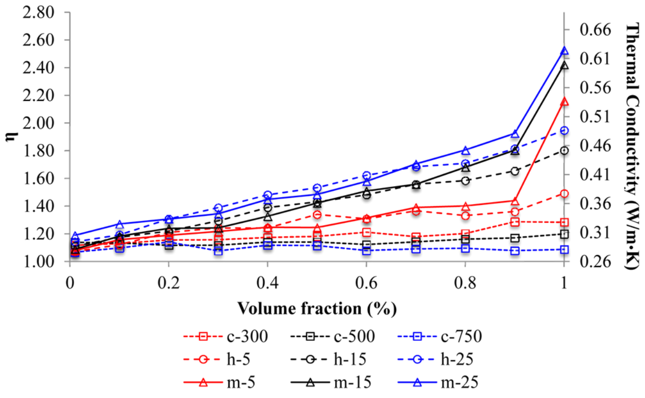

a) Thermal conductivity enhancement in the dilute regime

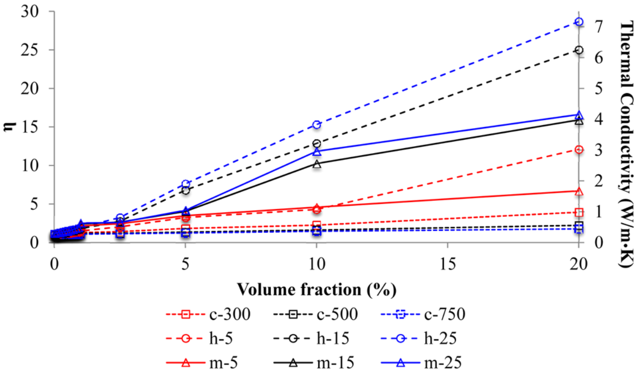

(b) Thermal conductivity enhancement in the percolating regime

Figure 1. Thermal conductivity enhancement of paraffin as a function of graphene nanoparticle concentration, geometry, and type.

In parts a and b of Figures 1, η represents the thermal conductivity enhancement factor (k_e/k_{PCM}). The thermal conductivity of the graphene−paraffin nanocomposites shows a higher dependence on the graphene constriction geometry in the percolating regime than it does when the nanoparticles exist in the dilute regime (Figure 1a vs Figure 1b); in other words, heat flow is more sensitive to the size of the constriction formed between graphene interfaces than it is to the area at the graphene−paraffin interfaces. This is particularly noticeable at higher volume concentrations. Nevertheless, it is clear from Figure 1a,b that the geometry (diameter, thickness) of the graphene nanoparticle significantly influences the bulk thermal conductivity of the paraffin, regardless of whether the nanoparticles percolate. For instance, a comparison between the effects of the h-5 and m-5, the h-15 and m-15, and the h-25 and m-25 type graphene nanoparticles on the thermal conductivity enhancement of paraffin in the dilute regime suggests that when the nanoparticles are completely separated from one another, the nanoparticle's diameter (or lateral

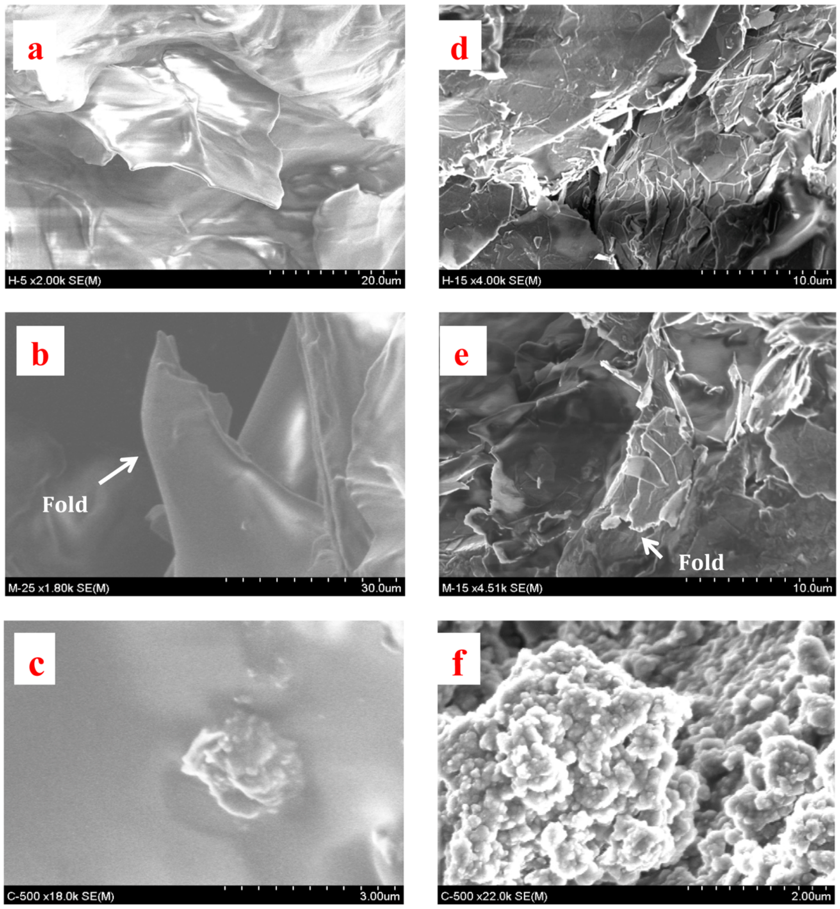

Figure 2. Morphology of graphene−paraffin composites characterized using scanning electron microscopy: (a) h-5 graphene−paraffin (dilute), (b) m-25 graphene−paraffin (dilute), (c) c-500 graphene−paraffin (dilute), (d) h-15 graphene−paraffin (percolating), (e) M-15 graphene−paraffin (percolating), (f) c-500 graphene−paraffin (percolating).

dimension) has a significant effect on thermal conductivity, with larger lateral dimensions corresponding to higher thermal conductivities. Additionally, examination of the different c-type nanoparticle composites in the dilute regime suggests that the layer thickness has a significant effect on the thermal conductivity, where an increase in n corresponds to an increase in the thermal conductivity of the composite. The effect of layer thickness is further illustrated in the percolating regime (Figure 1b), where a larger number of graphene layers correspond to a higher thermal conductivity.

In isolation, the significant impacts of graphene layer number and diameter reported here help to explain the wide range of thermal conductivities reported previously for graphene nanocomposites.[22,34] Additionally, the h-25 type, randomly organized graphene nanoparticles actually outperform current state-of-the-art aligned MWCNT-based composite materials by a factor of 1.6 at 20 vol %.[29] Moreover, the simple and cost-effective materials synthesis techniques used to fabricate these nanocomposite PCMs, in tandem with the superior thermal conductivity achieved by the h-25 type graphene nanoparticles, might make these materials more attractive candidates than state-of-the-art graphene foams, which have been shown to achieve η up to 18 at very low volume concentrations (∼1−2 vol %).[8] Although the graphene foams in ref 3 may not displace much of the PCM, leading to greater usability of its latent heat, the extremely small pore sizes are expected to suppress natural convection and, therefore, may outweigh the benefit provided by the enhanced thermal conductivity of the PCM. However, while the superior thermal conductivity achieved through the insertion of graphene nanoparticles into a PCM in this work can serve as a benchmark moving forward, it remains important to understand whether these enhancements have been maximized and, if not, to understand what physical mechanisms are responsible for impeding heat flow within graphene nanocomposite PCMs.

To determine whether the thermal conductivity of the PCM has been maximized in the presence of the graphene nanoparticles used in this work, the data in Figure 1 is evaluated and compared to what is predicted using the mixing approximation in eq 1. For instance, the thermal conductivity enhancements of paraffin due to the presence of isolated c-type graphene nanofillers (Figure 1a) suggest that as the thickness of the c-type nanoparticle increases, the bulk thermal conductivity of the paraffin also increases. Upon increasing the layer number from 3 to 20 to 44, this trend continues. These results possibly indicate that the intrinsic thermal conductivity of the graphene nanoparticles scales as $k_{\text{graphene}} \sim \ln(n)$ and is below the thermal conductivity of graphite (rather than several times greater, as is the case for suspended graphene[34]). This leads one to assume that the suppression of ZA phonons in graphene by the surrounding paraffin is primarily responsible for these underwhelming results. However, the mixing approximation given in eq 1 still predicts at least an order of magnitude higher thermal conductivity enhancement than what is found for the nanocomposites in this work, even when accounting for a reduction in the intrinsic thermal conductivity of graphene due to the suppression of ZA phonons. According to Figure 1, the highest thermal conductivity enhancement achieved by any of the nanoparticles at a 20 vol % loading level is roughly $\eta \sim 25$ (for the h-25 type graphene). However, if one assumes that the intrinsic thermal conductivity of h-25 graphene is as low as 100 W/mK (which is much lower than results obtained for atomically thick graphene on SiO_2[26] and thus represents a conservative approximation of its actual value given the $k \sim \ln(n)$ dependence of supported graphene and the 44 layers present in the h-25 graphene), the enhancement shown in Figure 1b should still be a factor of at least 10 greater than what is reported in this work.

To identify additional mechanisms that limit thermal transport within graphene–paraffin nanocomposites, we turn to observations of the graphene nanoparticle morphology within the paraffin. These observations allow us to better understand the underlying physical mechanisms that might cause such a significant divergence from the expected thermal conductivity enhancements predicted by eq 1. Images of graphene nanoparticles embedded within paraffin are shown in Figure 2. It should be noted that the graphene nanoparticles are coated in paraffin; thus, their exact geometries cannot be directly extrapolated from these images.

Parts a–c of Figure 2 show the morphology of isolated h-type, m-type, and c-type graphene nanoparticles embedded within paraffin using scanning electron microscopy (SEM). Details of the methods used for SEM imaging are given in the Experimental Methods section. Distinct differences exist between the morphology of the h-type graphene nanoparticle shown in Figure 2a and the m- and c-type nanoparticles in Figure 2b,c). In Figure 2a, the h-type graphene nanoparticle is coated with paraffin and remains mechanically rigid within the composite. However, when the graphene nanoparticle thickness is reduced to 7 nm (Figure 2b), it begins to fold. It should be noted that although only a single micrograph is provided here, flexural bending of the m-type graphene was confirmed in 90% of the images taken for this work; however, the degree to which the graphene folded within the composite was not possible to obtain due to the nature of the brittle fracture method used for imaging. Nevertheless, there is sufficient evidence to suggest that there is significant bending of the m-type nanoparticles within the PCM.

A further reduction in thickness down to 2 nm results in significant "wrinkling" of the graphene nanoparticle, analogous in many ways to a sheet of paper that has been wadded up. This phenomenon was found to occur in all of the samples that were imaged. Within the context of heat conduction, the c-type graphene nanoparticles result in the lowest thermal conductivity enhancement of any graphene nanoparticle type and is over an order of magnitude lower than what is calculated using eq 1. Supported by the micrographs in Figures 2a–c, one possible explanation for this disappointing result is that there is an increased number of interfaces across thinner graphene nanoparticles, which leads to a high rate of interfacial phonon scattering. The increase in folding that is seen in Figures 2a–c is readily explained by the bending stiffness values in Table 2.

Figure 1b depicts the thermal conductivity enhancement of paraffin due to the presence of percolating networks of graphene. In this case, the thermal enhancement factor ranges from $\eta \sim 2$ to ~ 25 at 20 vol %. Similar to the thermal conductivity enhancements in the dilute regime, the effective thermal conductivity of the paraffin nanocomposite is found to increase with increasing graphene nanoparticle thickness and diameter. Additionally, this result remains far shy of what standard mixing theory predicts for the thermal conductivity enhancement of paraffin due to the incorporation of percolating graphene nanoparticles. Unlike the thermal conductivity enhancement of the paraffin–graphene nanocomposites in the dilute regime (Figure 1a), however, all three types of nanoparticles exhibit considerably different thermal conductivity enhancements when the graphene percolates throughout the paraffin. Thus, an examination of the network's morphology is critical in order to understand the underlying physical mechanisms that govern the flow of heat across it.

Figure 2 depicts the 15 nm thickness, h-type nanoparticles embedded within the paraffin (Figure 2d), the 7 nm thickness m-type nanoparticles embedded within the paraffin (Figure 2e), and the 2 nm thickness c-type nanoparticles embedded within the paraffin (Figure 2f), each at 20 vol %. In Figure 2f, one observes that the previously self-folded c-type graphene nanoparticles cluster together, which creates an even higher number of interfaces for phonons to scatter across. Accordingly, the c-type graphene nanoparticles provide a lower paraffin thermal conductivity enhancement than either the h-type or m-type graphene nanoparticles, as shown in Figure 1a. Unlike the thermal conductivity enhancement in the dilute limit, however, the enhancement provided by the h-type and m-type nanoparticles begins to diverge as a function of volume loading level in the percolating regime, as shown in Figure 1b. In this case, the bulk thermal conductivity of the paraffin is higher when the h-type graphene nanofillers ($n = 44$) are used than when the m-type graphene nanofillers are used ($n = 20$), possibly validating the aforementioned $k_{\text{graphene}} \sim \ln(n)$ dependence. An alternate explanation for this finding is that while the folding of m-type graphene does not severely impede the flow of heat when graphene is only in contact with paraffin, it does significantly increase the number of interfaces within the PCM when it folds across nanoparticle–nanoparticle junctions (as shown in Figure 2e). The increase in the number of junctions across the m-type nanoparticle network is therefore expected to result in a higher rate of phonon boundary scattering. This increased rate of phonon boundary scattering will subsequently reduce the heat flow rate from one graphene nanoparticle to another. At present, however, it is not understood whether the bending of the m-type and c-type nanoparticles is more responsible for their underwhelming performance in PCMs than the reduction of the intrinsic thermal conductivity of the graphene nanoparticles.

To determine what mechanisms are most responsible for limiting the thermal enhancement of PCMs embedded with graphene nanoparticles, nanoscale thermal phenomena are analyzed by calculating the interfacial thermal resistance across both graphene–paraffin and graphene–graphene interfaces for each type of graphene nanoparticle using the model developed by Chu et al.[35] To do this, we apply a best-fit curve (eq 2) for each distribution in Figure 1 and extract R_k from eq 4.

$$\frac{k_e}{k_m} = \frac{2/3[f - 1/p]^{\alpha}}{H(p) + 1/((k_x/k_m) - 1)} + 1 \tag{2}$$

where

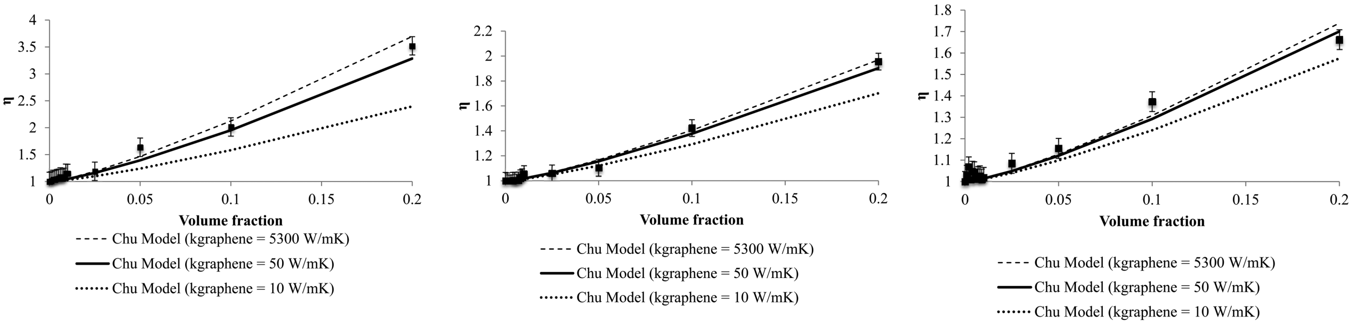

(a) c-300 type graphene nanoparticles (b) c-500 type graphene nanoparticles (c) c-750 type graphene nanoparticles

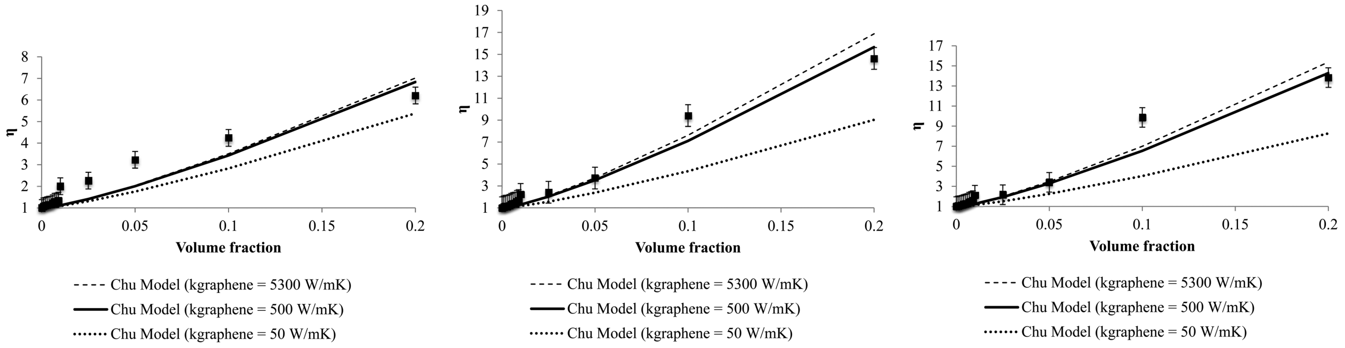

(d) m-5 type graphene nanoparticles (e) m-15 type graphene nanoparticles (f) m-25 type graphene nanoparticles

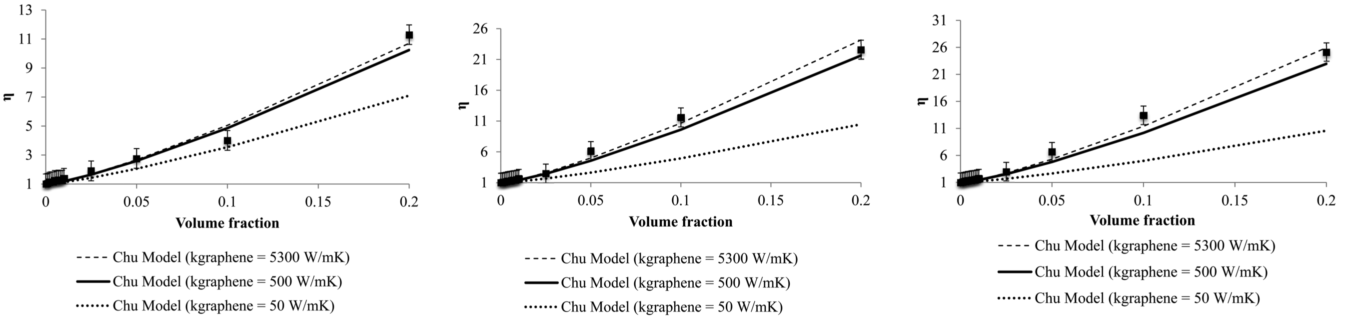

(g) h-5 type graphene nanoparticles (h) h-15 type graphene nanoparticles (i) h-25 type graphene nanoparticles

Figure 3. Influence of intrinsic graphene nanoparticle thermal conductivity on best-fit curves for the model developed by Chu et al. for each of the composites synthesized in this work.

$$H(p) = \frac{\ln\left(p + \sqrt{(p^2 - 1)}\right) \times p}{\sqrt{(p^2 - 1)^3}} - \frac{1}{p^2 - 1} \tag{3}$$

$$k_x = \frac{k_{\text{graphene}}}{2 \cdot R_k \cdot (k_{\text{graphene}}/L) + 1} \tag{4}$$

In eqs 2, 3, and 4, k_e is the effective thermal conductivity of the nanocomposite (W/mK), k_m is the thermal conductivity of the PCM (W/mK), f is the volume fraction of graphene nanoparticles, α is a dimensionless fitting parameter, k_{graphene} is the intrinsic thermal conductivity of graphene, R_k is the effective thermal resistance at an individual graphene nanoparticle's boundary (m^{2}K/W), and L is the characteristic diameter of the nanoparticle (m). The goal of this analytical work is to extract R_k from eq 4 in order to make relative comparisons of the graphene–paraffin and graphene–graphene interfacial thermal resistance between the different types of graphene nanoparticles listed in Table 2. For the dilute regime, α is assumed to have a value of 1 based on the expected linearity of the trend that describes the thermal conductivity enhancement of nanocomposites as a function of nanoparticle volume fraction.[36,37] This makes for a simple and direct calculation of R_k from eq 4. For the percolating regime, however, the choice of α is not straightforward. Consequently, we first assume that the intrinsic thermal conductivity of graphene (k_{graphene}) is 5300 W/mK and then solve for α. Subseqently, the intrinsic thermal conductivity of graphene is varied from 10 W/mK to 5300 W/mK in order to determine whether the intrinsic thermal conductivity of graphene has a more significant effect on thermal transport within the composite (i. e., large deviations compared to the original distribution at k_{graphene} = 5300 W/mK) than the interfacial thermal resistance. These deviations are shown in Figure 3 for each type of nanocomposite.

In Figure 3a–c, it is shown that even after a 2-order of magnitude decrease in the intrinsic thermal conductivity of graphene (from 5300 to 50 W/mK), the best-fit curve does not vary by more than 5%. Given that the intrinsic thermal conductivity of graphene is not expected to decrease by more than this amount (due to a better match in the phonon density of states between paraffin and carbon than between SiO_2 and carbon),[14,15,17,18,26] it is clear that the mechanism most responsible for the underwhelming performance of graphene-based nanocomposite PCMs is the interfacial thermal resistance across the faces of graphene nanoparticles. With the expected $k \sim \ln(n)$ dependence of thermal conductivity on graphene layer number,[38] it can also be inferred that the physical mechanism limiting the expected thermal enhancement within all of the graphene nanocomposite PCMs in this study is the interfacial thermal resistance between individual graphene nanoparticles.

The interfacial thermal resistance is quantified in Figure 4 using the best-fit curves generated in Figure 3a–i. For this analysis, it is assumed that the nanoparticle intrinsic thermal conductivity takes the form $k \sim \ln(n)$ and that their actual values are similar to or greater than those obtained for graphene embedded in SiO_2 for the reasons mentioned previously. It should also be noted that if the intrinsic thermal conductivity of the graphene were to scale according to the data supplied by Ghosh et al.,[39] the results presented in this work would remain valid and would further strengthen those presented in Figure 4. This is primarily due to the expectation that the c-type nanoparticles would provide the largest thermal enhancement to bulk paraffin because they have the lowest value of thickness and therefore the highest thermal conductivity (the intrinsic thermal conductivity of suspended graphene is found to increase with decreasing layer number[15,39]).

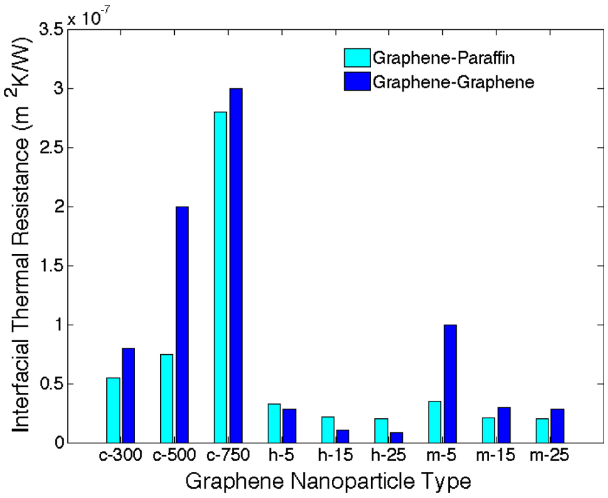

Figure 4. Nanoscale interfacial thermal resistance at graphene–paraffin interfaces (light-blue bars) and graphene–graphene interfaces (dark-blue bars).

As expected, the graphene–paraffin interfacial thermal resistance is lower than the graphene–graphene interfacial thermal resistance for both the c-type and m-type graphene nanoparticles. This is primarily due to the propensity for the graphene to create a large number of interfaces in the percolating regime for each of these two types of nanoparticles, thereby increasing the magnitude of phonon scattering within the composite. In fact, only the h-type graphene exhibits a lower interfacial thermal resistance between nanoparticle interfaces than between graphene–paraffin interfaces due to its propensity to remain mechanically rigid in both the dilute and percolating regimes. This is also the only graphene nanoparticle type that abides by the acoustic and diffuse mismatch models,[40,41] which suggest that there is a greater resistance to heat flow between two dissimilar materials than between two similar materials. Additionally, these results quantitatively illustrate that the folding experienced by the thinner graphene nanoparticles significantly increases the thermal boundary resistance at graphene interfaces. In fact, the interfacial thermal resistance calculated in this work is ~1 order of magnitude higher than that which is found for graphene–paraffin interfaces using molecular dynamics simulations when graphene is assumed to be mechanically rigid.[18,34] In tandem with the data supplied in Figure 3, these results suggest that the graphene layer number (and thus its mechanical rigidity) is most responsible for impeding heat flow within graphene-based nanocomposites. Consequently, this work illustrates the difficulty in achieving optimal enhancements of the thermal properties of PCMs with graphene nanoparticles using cost-effective fabrication methods and offers significant insight into the physical mechanisms that currently limit heat flow in nanocomposite PCMs, which are critical for their successful design and implementation in future energy systems and electronic devices.

■ CONCLUSIONS

In this study, the thermal conductivity enhancement of paraffin due to the presence of high thermal conductivity graphene nanoparticles is shown to increase with increasing graphene thickness and diameter. This explains the wide variability in the thermal conductivity enhancement of bulk materials in the literature with different types of graphene nanoparticles. In this work, η is found to vary from ~2 to ~25 at 20 vol % for graphene whose number of layers range from n = 3–44. Qualitative visualization and analytical evaluations of the thermal resistance across graphene interfaces confirmed that the thinner graphene nanoparticles produced an increased number of interfaces due to folding within the paraffin and that these folds resulted in increased phonon boundary scattering at both the graphene–paraffin interfaces and across the graphene nanoparticle networks. Consequently, this work reveals that the thermal conductivity enhancement of paraffin phase change materials due to the presence of graphene nanoparticles is a stronger function of the bending stiffness of the graphene than its intrinsic thermal conductivity. It is expected that this work will open new areas of research regarding the combined effects of nanoparticle mechanics and their intrinsic thermal transport properties on the thermal conductivity of graphene enhanced PCMs.

■ EXPERIMENTAL METHODS

Materials Synthesis. Randomly oriented graphene–paraffin nanocomposites were synthesized using a two-step technique. Graphene was first deposited in a melted paraffin wax (T_{melt} = 329.15 K) at concentrations ranging from 0.01 to 20 vol % and was subsequently dispersed using a sonic horn. An ultrasonic pulse iwas continuously operated at 32 Hz for a duration of 20 min with each sample. The resulting liquid paraffin composite material was poured into two separate cylindrical molds (diameter = 2.8 cm, height = 1.4 cm) resting on a polished stainless steel substrate. The mirror finish on the stainless steel substrate was designed to minimize the surface roughness of the face of the solid composite that directly touched the Transient Plane Source sensor in order to minimize the thermal interface resistance between the sensor and the surrounding material (though it should be noted this effect can be eliminated by adjusting the starting time for the Transient Plane Source curve fit procedure, which is described briefly in the next section and in detail in other work).[42,43] The liquid paraffin composite was poured into the mold in several layers in order to eliminate air gaps within the material.

Scanning Electron Microscopy. Scanning electron microscopy (SEM, Hitachi S-4800) was used to delineate between the morphology of the nanoparticles within paraffin at different volume loading levels. SEM was performed on the sample using the techniques described in Warzoha et al.[5,13] Briefly, a brittle fracture was performed on each of the samples synthesized for this work in order to avoid significant displacement of graphene nanoparticles within the paraffin. Frictional forces from traditional cutting techniques were found to result in extremely high local temperatures at the paraffin−instrument interface, which melts the paraffin in close proximity to the cut and alters the distribution of graphene nanoparticles.

Transient Plane Source Measurements. The thermal conductivity of each few-layer graphene−paraffin nanocomposite was measured using a Transient Plane Source device. The details of this measurement technique and its use for measuring the thermal conductivity of nanocomposites are detailed elsewhere.[44] Briefly, a sensor was used as both a heat source and a transient temperature thermometer in order to measure the temperature rise in a surrounding material as a function of heat flux at the sensor interface. The sensor was either sandwiched between two solid materials or was immersed within a liquid material. In theory, when the temperature rise of the sensor is large with respect to time, the surrounding material behaves as a thermal insulator, whereas when the temperature rise is relatively low, the surrounding material behaves as a thermal conductor.

A number of different physical phenomena are known to affect the accuracy of this measurement technique. First, it is critical that the thermal penetration depth ($\Delta p = 2\cdot(\alpha\cdot t)^{1/2}$, where α is the thermal diffusivity of the surrounding material and t is the total time that the test is run for) does not exceed the physical system boundaries; in other words, the material must be spatially "infinite" during the transient measurement period or else the user runs the risk of thermal interference due to the presence of some thermal impedance at the material's boundary. In this work, the samples are cylindrical with diameters and heights of 2.8 and 1.4 cm, respectively. Given that the radius of the Transient Plane Source sensor is 3.189 mm, the maximum allowable thermal penetration depth in any direction is 1.08 cm. The maximum thermal penetration depth that is for any test in this study is calculated to be 0.98 cm, which is shy of the maximum allowable thermal penetration depth by 0.1 cm.

In addition to the geometric constraints imposed upon the materials used during measurement, it has previously been shown that the accuracy of this measurement technique is dependent on a "characteristic" time ($t_c = r^2/\alpha$, where r is the radius of the sensor). When the characteristic time is between $0.33 \le t_c \le 1.0$, the solution to the differential equation describing heat flow from the sensor to the surrounding material is insensitive to the curve fitting procedures that are used to relate the data to the solution for the nonlinear differential equation.[44] However, measurements outside of this time window can result in significant error when calculating a solution for the thermal conductivity of the surrounding material. The characteristic time for all of the samples tested in this study was kept within this range in order to ensure that the curve fitting procedure was accurately applied to the data obtained for each sample.

Prior to testing, the Transient Plane Source device was calibrated using two materials with contrasting thermal conductivities that are within the range of expected values for the nanocomposites used in this study (stainless steel 316, 14.2 W/m·K, and polystyrene, 0.028 W/m·K). The Transient Plane Source manufacturer supplies the user with both calibration materials. The thermal conductivity of each calibration material was tested by using the Transient Plane Source device and each was determined to be within ±1% of the data supplied by the manufacturer (see Supporting Information). Nanocomposites have previously been tested using this technique and compared to several other standard techniques.[45] We found that the Transient Plane Source technique produced values for the thermal conductivity of various nanocomposites that were within the uncertainty of a variety of standard techniques.

■ ASSOCIATED CONTENT

Ⓢ Supporting Information

Additional information detailing the calibration of the thermal conductivity measurement apparatus, the calculation of the percolation thresholds for each nanocomposite PCM, and additional SEM images. This material is available free of charge via the Internet at http://pubs.acs.org.

■ AUTHOR INFORMATION

Corresponding Author

*E-mail: amy. fleischer@villanova. edu.

Present Address

[†]United States Naval Academy, 121 Blake Road, Annapolis, Maryland 21402, United States. E-mail: ronald. warzoha@gmail. com.

Notes

The authors declare no competing financial interest.

■ ACKNOWLEDGMENTS

We appreciate the support of the National Science Foundation (CBET1235769) and the Environmental Protection Agency Science to Achieve Results (STAR) Fellowship. Any opinions, findings, and conclusions or recommendations expressed in this material are those of the author(s) and do not necessarily reflect the views of the National Science Foundation. The research described in this paper has also been funded in part by the United States Environmental Protection Agency (EPA) under the Science to Achieve Results (STAR) Graduate Fellowship Program. EPA has not officially endorsed this publication and the views expressed herein may not reflect the views of the EPA.

■ REFERENCES

(1) Chintakrinda, K.; Warzoha, R. J.; Weinstein, R. D.; Fleischer, A. S. Quantification of the Impact of Embedded Graphite Nanofibers on the Transient Thermal Response of Paraffin Phase Change Material Exposed to High Heat Fluxes. *J. Heat Transfer* **2012**, *134*, 071901.

(2) Ehid, R.; Weinstein, R. D.; Fleischer, A. S. The Shape Stabilization of Paraffin Phase Change Material to Reduce Graphite Nanofiber Settling during the Phase Change Process. *Energy Convers. Manage.* **2012**, *57*, 60−67.

(3) Ehid, R.; Fleischer, A. S. Development and Characterization of Paraffin-Based Shape Stabilized Energy Storage Materials. *Energy Convers. Manage.* **2012**, *53*, 84−91.

(4) Warzoha, R. J.; Weigand, R.; Rao, A.; Fleischer, A. S. Experimental Characterization of The Thermal Diffusivity of Paraffin Phase Change Material Embedded with Herringbone Style Graphite Nanofibers. ASME Summer Heat Transfer Conference, Rio Grande, PR, July 8−12, 2012; pp 307−315.

(5) Warzoha, R.; Sanusi, O.; McManus, B.; Fleischer, A. S. Development of Methods to Fully Saturate Carbon Foam With Paraffin Wax Phase Change Material for Energy Storage. *J. Sol. Energy Eng.* **2012**, *135*, 021006.

(6) Chintakrinda, K.; Weinstein, R. D.; Fleischer, A. S. A Direct Comparison of Three Different Material Enhancement Methods on the Transient Thermal Response of Paraffin Phase Change Material Exposed to High Heat Fluxes. *Int. J. Therm. Sci.* **2011**, *50*, 1639−1647.

(7) Sanusi, O.; Warzoha, R.; Fleischer, A. S. Energy Storage and Solidification of Paraffin Phase Change Material Embedded with Graphite Nanofibers. *Int. J. Heat Mass Transfer* **2011**, *54*, 4429−4436.

(8) Ji, H.; Sellan, D. P.; Pettes, M. T.; Kong, X.; Ji, J.; Shi, L.; Ruoff, R. S. Enhanced Thermal Conductivity of Phase Change Materials with

Ultrathin-Graphite Foams for Thermal Energy Storage. *Energy Environ. Sci.* **2014**, *7*, 1185−1192.

(9) Saha, S. K.; Srinivasan, K.; Dutta, P. Studies on Optimum Distribution of Fins in Heat Sinks Filled With Phase Change Materials. *J. Heat Transfer* **2008**, *130*, 034505.

(10) Gallego, N. C.; Klett, J. W. Carbon Foams for Thermal Management. *Carbon* **2003**, *41*, 1461−1466.

(11) Pop, E.; Mann, D.; Wang, Q.; Goodson, K.; Dai, H. Thermal Conductance of an Individual Single-Wall Carbon Nanotube above Room Temperature. *Nano Lett.* **2006**, *6*, 96−100.

(12) Balandin, A. A.; Ghosh, S.; Bao, W.; Calizo, I.; Teweldebrhan, D.; Miao, F.; Lau, C. N. Superior Thermal Conductivity of Single-Layer Graphene. *Nano Lett.* **2008**, *8*, 902−907.

(13) Warzoha, R. J.; Weigand, R. M.; Fleischer, A. S. Temperature-Dependent Thermal Properties of a Paraffin Phase Change Material Saturated with Herringbone Style Graphite Nanofibers. *Appl. Energy* **2014**, DOI: 10.1016/j. apenenergy.2014.03.091.

(14) Babaei, H.; Keblinski, P.; Khodadadi, J. M. Improvement in Thermal Conductivity of Paraffin by Adding High Aspect-Ratio Carbon-Based Nano-Fillers. *Phys. Lett. A* **2013**, *377*, 1358−1361.

(15) Pop, E.; Varshney, V.; Roy, A. K. Thermal Properties of Graphene: Fundamentals and Applications. *MRS Bull.* **2012**, *37*, 1273−1281.

(16) Xiao, X.; Zhang, P. Morphologies and Thermal Characterization of Paraffin/carbon Foam Composite Phase Change Material. *Sol. Energy Mater. Sol. Cells* **2013**, *117*, 451−461.

(17) Babaei, H.; Keblinski, P.; Khodadadi, J. M. Thermal Conductivity Enhancement of Paraffins by Increasing the Alignment of Molecules through Adding CNT/graphene. *Int. J. Heat Mass Transfer* **2013**, *58*, 209−216.

(18) Goli, P.; Legedza, S.; Dhar, A.; Salgado, R.; Renteria, J.; Balandin, A. A. Graphene-Enhanced Hybrid Phase Change Materials for Thermal Management of Li-Ion Batteries. *J. Power Sources* **2014**, *248*, 37−43.

(19) Hung, M.-T.; Choi, O.; Ju, Y. S.; Hahn, H. T. Heat Conduction in Graphite-Nanoplatelet-Reinforced Polymer Nanocomposites. *Appl. Phys. Lett.* **2006**, *89*, 023117.

(20) Fang, X.; Fan, L.-W.; Ding, Q.; Wang, X.; Yao, X.-L.; Hou, J.-F.; Yu, Z.-T.; Cheng, G.-H.; Hu, Y.-C.; Cen, K.-F. Increased Thermal Conductivity of Eicosane-Based Composite Phase Change Materials in the Presence of Graphene Nanoplatelets. *Energy Fuels* **2013**, *27*, 4041−4047.

(21) Fan, L.-W.; Fang, X.; Wang, X.; Zeng, Y.; Xiao, Y.-Q.; Yu, Z.-T.; Xu, X.; Hu, Y.-C.; Cen, K.-F. Effects of Various Carbon Nanofillers on the Thermal Conductivity and Energy Storage Properties of Paraffin-Based Nanocomposite Phase Change Materials. *Appl. Energy* **2013**, *110*, 163−172.

(22) Shahil, K. M. F.; Balandin, A. A. Thermal Properties of Graphene and Multilayer Graphene: Applications in Thermal Interface Materials. *Solid State Commun.* **2012**, *152*, 1331−1340.

(23) Shahil, K. M. F.; Balandin, A. A. Graphene-Multilayer Graphene Nanocomposites as Highly Efficient Thermal Interface Materials. *Nano Lett.* **2012**, *12*, 861−867.

(24) Moore, A. L.; Shi, L. Emerging Challenges and Materials for Thermal Management of Electronics. *Mater. Today* **2014**, 1−12.

(25) Klemens, P. G. Theory of Thermal Conduction in Thin Ceramic Films. *Int. J. Thermophys.* **2001**, *22*, 265−275.

(26) Seol, J. H.; Jo, I.; Moore, A. L.; Lindsay, L.; Aitken, Z. H.; Pettes, M. T.; Li, X.; Yao, Z.; Huang, R.; Broido, D.; Mingo, N.; Ruoff, R. S.; Shi, L. Two-Dimensional Phonon Transport in Supported Graphene. *Science* **2010**, *328*, 213−216.

(27) Warzoha, R. J.; Zhang, D.; Feng, G.; Fleischer, A. S. Engineering Interfaces in Carbon Nanostructured Mats for the Creation of Energy Efficient Thermal Interface Materials. *Carbon* **2013**, *61*, 441−457.

(28) Marconnet, A. M.; Panzer, M. A.; Goodson, K. E. Thermal Conduction Phenomena in Carbon Nanotubes and Related Nanostructured Materials. *Rev. Mod. Phys.* **2013**, *85*, 1295−1326.

(29) Marconnet, A.; Yamamoto, N.; Panzer, M. A.; Wardle, B. L.; Goodson, K. E. Thermal Conduction in Aligned Carbon Nanotube−Polymer Nanocomposites with High Packing Density. *ACS Nano* **2011**, *6*, 4818−4825.

(30) Huxtable, S. T.; Cahill, D. G.; Shenogin, S.; Xue, L.; Ozisik, R.; Barone, P.; Usrey, M.; Strano, M. S.; Siddons, G.; Shim, M.; Keblinski, P. Interfacial Heat Flow in Carbon Nanotube Suspensions. *Nature Mater.* **2003**, *2*, 731−734.

(31) Warzoha, R. J.; Fleischer, A. S. Heat Flow at Nanoparticle Interfaces. *Nano Energy* **2014**, *6*, 137−158.

(32) Wei, Y.; Wang, B.; Wu, J.; Yang, R.; Dunn, M. L. Bending Rigidity and Gaussian Bending Stiffness of Single-Layered Graphene. *Nano Lett.* **2013**, *13*, 26−30.

(33) Cranford, S.; Sen, D.; Buehler, M. J. Meso-Origami: Folding Multilayer Graphene Sheets. *Appl. Phys. Lett.* **2009**, *95*, 123121.

(34) Balandin, A. A. Thermal Properties of Graphene and Nanostructured Carbon Materials. *Nature Mater.* **2011**, *10*, 569−581.

(35) Chu, K.; Jia, C.; Li, W. Effective Thermal Conductivity of Graphene-Based Composites. *Appl. Phys. Lett.* **2012**, *101*, 121916.

(36) Marconnet, A. M.; Yamamoto, N.; Panzer, M. A.; Wardle, B. L.; Goodson, K. E. Thermal Conduction in Aligned Carbon Nanotube−Polymer Nanocomposites with High Packing Density. *ACS Nano* **2011**, *5*, 4818−4825.

(37) Nan, C.-W.; Birringer, R.; Clarke, D. R.; Gleiter, H. Effective Thermal Conductivity of Particulate Composites with Interfacial Thermal Resistance. *J. Appl. Phys.* **1997**, *81*, 6692.

(38) Chen, J.; Zhang, G.; Li, B. Substrate Coupling Suppresses Size Dependence of Thermal Conductivity in Supported Graphene. *Nanoscale* **2013**, *5*, 532−536.

(39) Ghosh, S.; Bao, W.; Nika, D. L.; Subrina, S.; Pokatilov, E. P.; Lau, C. N.; Balandin, A. A. Dimensional Crossover of Thermal Transport in Few-Layer Graphene. *Nature Mater.* **2010**, *9*, 555−558.

(40) Prasher, R. Acoustic Mismatch Model for Thermal Contact Resistance of van Der Waals Contacts. *Appl. Phys. Lett.* **2009**, *94*, 041905.

(41) Hopkins, P. E.; Duda, J. C.; Norris, P. M. Anharmonic Phonon Interactions at Interfaces and Contributions to Thermal Boundary Conductance. *J. Heat Transfer* **2011**, *133*, 062401.

(42) Warzoha, R. J.; Fleischer, A. S. Determining the Thermal Conductivity of Liquids Using the Transient Hot Disk Method. Part I: Establishing Transient Thermal-Fluid Constraints. *Int. J. Heat Mass Transfer* **2014**, *71*, 779−789.

(43) Warzoha, R. J.; Fleischer, A. S. Determining the Thermal Conductivity of Liquids Using the Transient Hot Disk Method. Part II: Establishing an Accurate and Repeatable Experimental Methodology. *Int. J. Heat Mass Transfer* **2014**, *71*, 790−807.

(44) Bohac, V.; Gustavsson, M. K.; Kubicar, L.; Gustafsson, S. E. Parameter Estimations for Measurements of Thermal Transport Properties with the Hot Disk Thermal Constants Analyzer. *Rev. Sci. Instrum.* **2000**, *71*, 2452.

(45) Buongiorno, J.; Venerus, D. C.; Prabhat, N.; Mckrell, T.; Townsend, J.; Christianson, R.; Tolmachev, Y. V.; Keblinski, P.; Hu, L.; Alvarado, J. L.; et al. A Benchmark Study on the Thermal Conductivity of Nanofluids. *J. Appl. Phys.* **2009**, *106*, 094312.